



Imaging slow failure in triaxially deformed Etna basalt using 3D acoustic-emission location and X-ray computed tomography

Philip M. Benson,^{1,2} Ben D. Thompson,² Philip G. Meredith,¹ Sergio Vinciguerra,³ and R. Paul Young²

Received 8 November 2006; revised 18 December 2006; accepted 26 December 2006; published 6 February 2007.

[1] We have deformed basalt from Mount Etna (Italy) in triaxial compression tests under an effective confining pressure representative of conditions under a volcanic edifice (40 MPa), and at a constant strain rate of $5 \times 10^{-6} \text{ s}^{-1}$. Despite containing a high level of pre-existing microcrack damage, Etna basalt retains a high strength of 475 MPa. We have monitored the complete deformation cycle through contemporaneous measurements of axial strain, pore volume change, compressional wave velocity change and acoustic emission (AE) output. We have been able to follow the complete evolution of the throughgoing shear fault without recourse to any artificial means of slowing the deformation. Locations of AE events over time yields an estimate of the fault propagation velocity of between 2 and 4 mm.s^{-1} . We also find excellent agreement between AE locations and post-test images from X-ray microtomography scanning that delineates deformation zone architecture. **Citation:** Benson, P. M., B. D. Thompson, P. G. Meredith, S. Vinciguerra, and R. P. Young (2007), Imaging slow failure in triaxially deformed Etna basalt using 3D acoustic-emission location and X-ray computed tomography, *Geophys. Res. Lett.*, 34, L03303, doi:10.1029/2006GL028721.

1. Introduction

[2] Quantitative understanding of the physical properties of volcanic rocks is becoming increasingly important in helping to unravel the complex deformation mechanisms acting within volcanic edifices; such as eruptive fracture opening, dome growth and propagation and flank stability [e.g., Voight and Elsworth, 1997; Elsworth and Day, 1999; Kilburn, 2003; Vinciguerra et al., 2005a]. Amongst such rocks, basalts are the most representative in forming active, effusive volcanoes. Emplacement at elevated temperature, either as extrusive bodies (lava flows) or intrusive bodies (dykes), followed by cooling, imposes thermal stresses that can lead to the evolution of crack damage [Vinciguerra et al., 2005a, 2005b]. This crack damage may exhibit anisotropy where the rock is subjected to anisotropic in-situ stress during emplacement [Benson et al., 2006].

[3] In turn, the occurrence and geometry of any induced network of crack damage will exert a large influence on the seismic signals routinely monitored at active volcanoes, such as Volcano-Tectonic (VT) events and Long Period (LP) events [McNutt, 1996; Chouet, 2003]. A link between the deformation processes, the resulting rock physical properties and these seismic characteristics may therefore help to elucidate the underlying mechanisms that generate such signals [e.g., Collier and Neuberg, 2006; Neuberg et al., 2006; Burlini et al., 2007]. However, details of the temporal evolution of damage and failure remain particularly poorly understood for rocks containing high levels of pre-existing damage. We have therefore studied the evolution of crack damage and failure in laboratory experiments on samples of Etna basalt. Previous studies on this material have shown that it is highly fractured, with commensurately low elastic wave velocities [Vinciguerra et al., 2005a]. Stanchits et al. [2006] have reported details of the accumulation of damage and failure under dry conditions. However, circulating fluids are ubiquitous in volcanic edifices, associated with hydrothermal activity, magmatic pressure and intense rainfall. We therefore present new results on the micromechanics of triaxial deformation and failure of water-saturated samples of Etna basalt using a novel combination of complementary techniques: advanced full waveform acoustic emission (AE) location, and post-test X-ray micro-tomography.

2. Sample Material

[4] Etna basalt is a porphyritic, alkali, lava-flow basalt from Mount Etna, Italy. It comprises millimetre-sized phenocrysts of pyroxene, olivine and feldspar in a fine-grained groundmass. The initial density of the block used in this study was 2860 kg/m^3 , and the initial porosity was 3.8%. Samples of 100mm length and 40 mm diameter were prepared using a diamond coring drill, with the end faces ground flat and parallel to within 0.01mm. This basalt was specifically chosen as previous studies have shown that it has a ubiquitous network of pre-existing microcracks [Vinciguerra et al., 2005b; Stanchits et al., 2006]. This microstructure is reflected in an anomalously low P-wave velocity of approximately 3250 m.s^{-1} (ambient conditions), and a relatively high permeability in the range 1 to $4 \times 10^{-17} \text{ m}^2$ at effective pressures from 5 to 50 MPa.

3. Experimental Equipment and Methods

[5] Deformation experiments were performed using a stiff, servo-controlled triaxial testing machine at University College London (UCL) [Eccles et al., 2005]. The apparatus

¹Mineral, Ice and Rock Physics Laboratory, Department of Earth Sciences, University College London, London, UK.

²Lassonde Institute, University of Toronto, Toronto, Ontario, Canada.

³High Pressure High Temperature Laboratory of Experimental Volcanology and Geophysics, Department of Seismology and Tectonophysics, Istituto Nazionale di Geofisica e Vulcanologia, Rome, Italy.

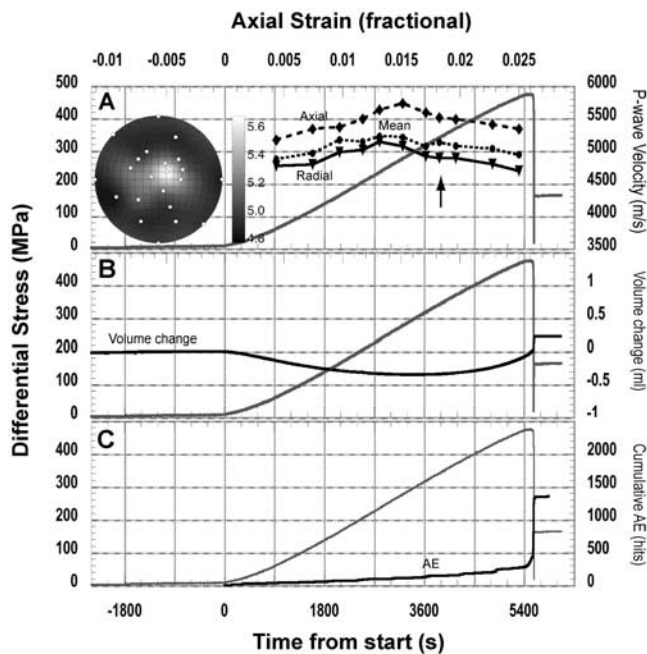


Figure 1. Stress-strain curve for water-saturated Etna basalt deformed at 40 MPa effective pressure, with other contemporaneous measurements superimposed. (a) Change in P-wave velocity and its anisotropy, (b) pore volume change, and (c) cumulative AE count. The arrow denotes the time at which the lower area stereographic projection of velocities was calculated.

is capable of achieving confining pressures ($\sigma_2 = \sigma_3$) of up to 400 MPa and a maximum principal axial stress (σ_1) of approximately 1.2 GPa across a 40 mm diameter sample [Eccles *et al.*, 2005]. For the experiments reported here, samples were deformed under fully drained conditions at a constant axial strain rate of $5 \times 10^{-6} \text{ s}^{-1}$, controlled via linear variable displacement transducers (LVDTs). A constant pore fluid pressure of 20 MPa was maintained throughout each experiment by means of two servo-controlled pore pressure intensifiers, which are also fitted with integral LVDTs that allows their use as volumeters. A rubber jacket separates the sample from the confining medium (silicone oil). A confining pressure of 60 MPa was used throughout, yielding an effective pressure of 40 MPa; conditions broadly representative of those at depth within a volcanic edifice.

[6] Elastic wave velocities and acoustic emissions (AEs) were measured using ten PZT crystals (of 1 MHz central frequency) mounted on stainless steel inserts embedded in the rubber jacket. Elastic wave velocity measurements were made using a Panametrics 5072PR pulser/receiver with received voltages pre-amplified by 40dB before being digitized and recorded on a Hyperion Giga-RAM recorder at 10 MHz sampling frequency [Thompson *et al.*, 2005, 2006]. The recorder is capable of storing 40 Gb of data on a circular Random Access Memory; equivalent to a moving window of the preceding 134s of full-waveform experimental data in the configuration described here. This is an important attribute, since the rapid acceleration to failure often observed in the final phase of triaxial deformation of brittle rocks is commonly accompanied by a supra-

exponential increase in AE activity [Meredith *et al.*, 1990]. This can cause conventional recorders to miss important events during the ‘mask-time’ required to transfer data from volatile memory to permanent storage.

[7] Whilst X-ray computed tomography has been a widely used technique in medical science for a number of years, it is relatively new in the geosciences. Medical scanners typically operate at a resolution in the millimetre range, and for rock deformation studies this is often insufficient. Furthermore, there can also be difficulties with power absorption in and maintaining focus through rock samples, which typically have higher densities than medical materials. More recently, however, higher resolution facilities have been purpose built for materials research, such as the High-Resolution X-ray Computed Tomography Facility at the University of Texas at Austin [Ketcham and Carlson, 2001], and a new generation of high-resolution instrumentation has entered the market such as microtomography (micro-CT) scanners. Although micro-CT scanning still has a somewhat lower resolution than, for example, confocal microscopy ($0.2 \mu\text{m}$ to $1 \mu\text{m}$) [Fredrich *et al.*, 1995], it has the benefit of being able to image relatively large volumes, and can therefore be an extremely useful tool for studying the 3D structure of crack and pore space [Louis *et al.*, 2006]. Post-failure imaging of the deformed samples from this study was done using a SkyScan-1172 X-ray microtomograph [Tricart *et al.*, 2000] (pixel resolution of $14 \mu\text{m}$) installed at the University of Toronto.

4. Experimental Results

[8] Figure 1 shows the mechanical data from one of our experiments on Etna basalt at an effective confining pressure of 40 MPa, together with P-wave velocity data, pore volume change and the cumulative AE count. The peak stress is high (approximately 475 MPa). This is followed by a post-peak period of strain softening and then a large stress drop. Elastic P-wave velocities were measured at intervals throughout the experiment along 24 ray-paths created by using 3 transmitters and 8 receivers. The change in velocity is plotted on Figure 1a for the axial and radial directions, and for the mean of all directions measured. Overall, all velocities increased with increasing differential stress up to about 275 MPa, (approximately 1.5% strain). Above this stress, all velocities decrease up to the point of dynamic failure which occurs at a strain of 2.64%.

[9] The P-wave velocity has an anisotropy of $\sim 8\%$ at 65 MPa, where cracks are already being closed normal to σ_1 . This increases during deformation to $\sim 13\%$ at 460 MPa, where new, dilatant cracks are growing parallel to σ_1 . It is likely that velocity anisotropy will increase further as failure is approached and the rate of dilatant cracking increases, as indicated by the acceleration in AE. A more detailed analysis of the anisotropy has been obtained by inverting the travel times along the 24 measurement ray-paths to determine the 3D velocity structure. A lower hemisphere projection taken at 370 MPa is given as the inset in Figure 1a, showing that the anisotropy can be characterized as horizontal transverse isotropy (HTI). The change in pore volume (Figure 1b) mirrors the change in P-wave velocity. It initially decreases as differential stress is increased, again reaching a minimum at a stress of approximately 275 MPa,

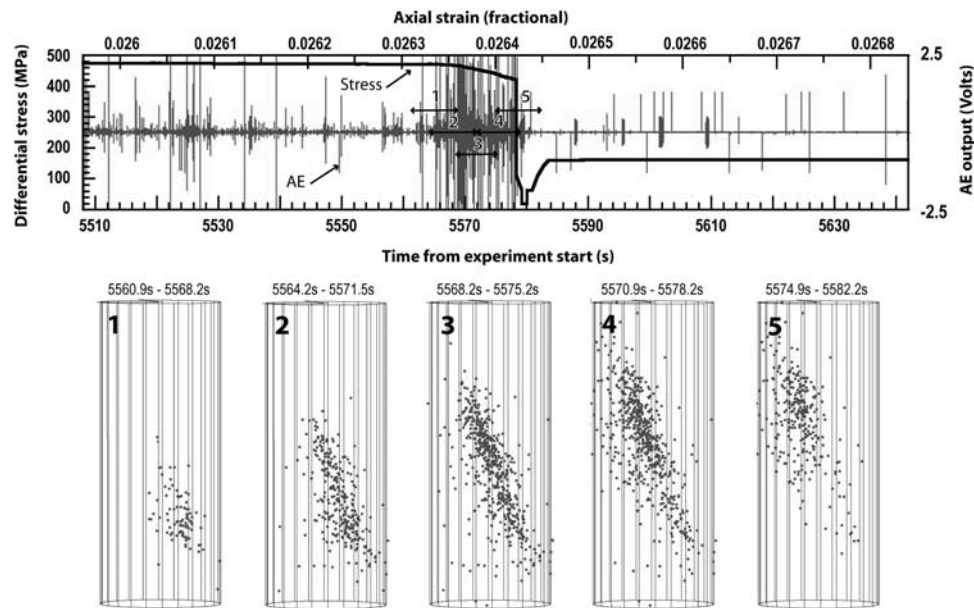


Figure 2. (top) The 134s continuous AE record of the strain softening and failure part of this test, with the stress/strain curve and the five AE location time windows superimposed. Evolution of the shear fault occurs over a period of approximately 22s. (bottom) AE event locations for the 5 overlapping time windows (1–5) harvested from the continuous record. Time spans are indicated above each figure.

and then increases up to the point of failure. Figure 1c shows the very low AE hit rate during the compactive period. It increases during the period of dilatant cracking, and accelerates dramatically during the period of strain softening between peak stress and dynamic failure.

[10] The continuous AE record (134 seconds, described earlier), has been used to analyze and image fault evolution and sample failure. The continuous record from 5508 s to 5642 s, which spans the period of fault growth and dynamic failure, is shown in Figure 2 (top) with the stress-strain curve superimposed. Note especially the high level of AE output associated with the decrease in differential stress that precedes dynamic failure. AE event data was extracted from the continuous record, using optimum levels of trigger threshold (40 mV) and record length (409.6 μ s) once the experiment had been completed. In total, 919 AE events were located, with a 2 mm accuracy, using a selection criterion of independent arrivals at 6 different transducers. This location error is calculated by multiplying the P-wave velocity model and associated picking error ($\sim 1\%$), by the RMS of the time residual between each measured arrival time, and the theoretical times calculated for that given location, averaged over the number of independent arrivals. A transversely isotropic simplex location algorithm was used, with a 5600 $\text{m}\cdot\text{s}^{-1}$ maximum (in the σ_1 direction) and 4850 $\text{m}\cdot\text{s}^{-1}$ minimum, measured from the 3D velocity structure shown earlier. Figure 2 (bottom, time windows 1–5) shows the evolution of the fault over a period of approximately 22s, shown as five overlapping 7s windows. The fault appears to nucleate in the lower right-hand part of the sample and then propagate to the upper left-hand part of the sample. As illustrated in Figure 1c, the bulk of the total acoustic emission activity from the whole experiment is contained within this 22 s period.

[11] Finally, Figure 3 shows images of the failed sample. The fault can be clearly seen in Figure 3a, running from bottom right to top left. Figure 3b shows the same image with located AE events superimposed as white dots. A central region through which the fault had propagated was chosen for micro-CT scanning, shown as a white rectangle on Figure 3b. The re-constructed micro-CT images are shown in plan and orthogonal elevations in Figures 3c, 3d, and 3e, with the AE data superimposed as black dots. The fault zone and a single large crack (X in Figure 3d) show up as light areas in these images, due to their lower local density. In the plan view (Figure 3d) the AE locations appear to exhibit a relatively large scatter relative to the width of the fault zone; however, this is simply an artifact occurring because all the AE data from the angled fault are projected onto this plane. By contrast, there is excellent agreement between the AE location data and the micro-CT image of the fault zone when viewed in elevation (Figure 3c). Taken together, this illustrates how 3D AE location data and micro-CT images can be used to provide complementary information about the evolution and structure of fault zones. While AE data can be used to follow the nucleation and propagation of the fault over time, the micro-CT images provide additional detail about the architecture of the fault zone and the distribution of damage within it, based on density contrasts.

5. Discussion and Conclusions

[12] Previous studies have shown that the Etna basalt used in this study contains a ubiquitous network of pre-existing microcracks, and ultrasonic wave velocity measurements suggest that these are distributed relatively isotropically [Vinciguerra *et al.*, 2005b]. Following other recent studies, [e.g., Benson *et al.*, 2006] we interpret

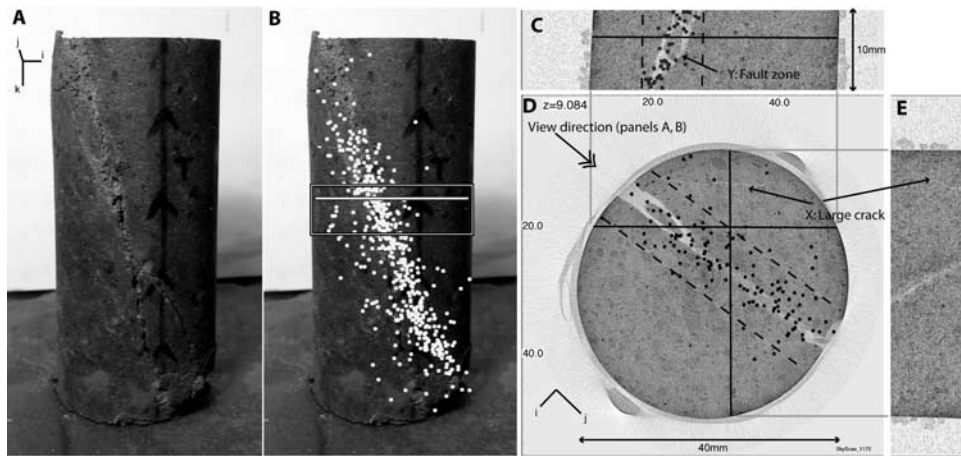


Figure 3. Sample of Etna basalt after failure showing. (a) The high level of crack damage and the throughgoing shear fault, and (b) the located AE events superimposed (white dots). A micro-CT scan of a central portion of the sample (gray box in Figure 2b) was performed. (d) Shows a cross-section along the line on the sample indicated in Figure 2b. Note that, in this 2D projection, the apparent fault zone extends to the dashed lines. (c and e) The fault can also be seen clearly on the two orthogonal planes (1st angle projection). See text for additional detail.

changes in elastic wave velocities as a proxy measure of crack damage. As differential stress was increased, all measured velocities initially increased, and the velocity anisotropy also increased (Figure 1a). This is consistent with earlier studies [e.g., *Ayling et al.*, 1995], and not only suggests that pre-existing crack damage is being closed, but also that cracks with their long axes normal to the σ_1 direction are being closed preferentially. However, above a differential stress of about 275 MPa (approximately 60% of the peak stress) all measured velocities decrease, suggesting the opening of new, dilatant microcracks. Velocity anisotropy continues to increase, and the velocity structure suggests HTI symmetry, consistent with the new cracks opening with their long axes parallel to the σ_1 direction. Pore volume change data (Figure 1b) is also consistent with this interpretation. The sample volume initially decreases and then reaches a minimum at the same values of strain and differential stress as those at which the P-wave velocities reach their maxima. The relatively low level of AE activity during this period further supports the idea of a pre-existing microcrack network (Figure 1c). At higher differential stress, the sample increases in volume so that at failure, it is larger than at the start of the experiment. We have then used the continuous AE record from the GigaRAM recorder to study the period from peak stress to dynamic failure in detail, as illustrated in Figure 2. Figure 2 (bottom, time window 1) shows a build-up in AE activity in period 1, immediately preceding peak stress, and that these events occur in a definite, off-axis, spatial cluster. During periods 2, 3 and 4, this cluster of AE propagates diagonally across the whole sample. These periods are coincident with the period of strain softening where the stress decreases from its peak value, and are characterized both by a large increase in AE rate and a large increase in AE magnitude. Only when the fault spans the complete sample does the dynamic stress drop that signifies macroscopic failure occur. Finally, period 5 encompasses this dynamic stress drop, and it is noteworthy that once the fault has propagated to the edge of the sample it appears to

leave a zone of quiescence behind it (Figure 2, bottom, time window 5).

[13] In this experiment, we have used our AE data to capture the complete process of nucleation and propagation of a localized fault zone, followed by dynamic failure and stress drop, in Etna basalt over an extended period of time (22 s). This has rarely been achieved before [*Lei et al.*, 2000; *Thompson et al.*, 2006], other than by artificially slowing the fault nucleation and propagation by means of closed-loop servo-control of the loading using AE as the feedback control [*Lockner et al.*, 1991]. Using the times and locations of the AE events in our propagating cluster, we have calculated a propagation speed via a simple least square fit to a 2D ellipse (using the criterion of 95% of data points inside the ellipse and with the major axis aligned along the sample). This gives a speed of $\sim 4 \text{ mm.s}^{-1}$ for the leading edge of the fault and $\sim 2 \text{ mm.s}^{-1}$ for the center. This is much slower than the speed of 17 mm.s^{-1} calculated for fault propagation in laboratory samples of Westerly granite by *Thompson* [2006]. Clearly, AE analysis of rock fracture and failure is highly dependent upon the speed and storage capacity of the advanced instrumentation used to capture AE events. However, we also partly attribute our ability to follow the complete deformation and failure in Etna basalt to the high level of pre-existing damage. Firstly, this provides a multitude of stress concentration points within the material which aids microcrack growth and extension. Secondly, it provides space for storage of pore water that allows subcritical crack growth processes such as stress corrosion to contribute to the deformation. Together, these features make the material deform in a less brittle manner, and act to slow the failure process in a natural rather than artificial way. The important point being that, by definition, the rate of crack growth during stress corrosion is “sub-critical” so that the rock fails at lower stress but much more slowly and over a much extended time period. This is exactly what we see.

[14] Our AE locations typically have an accuracy of 1 to 2 mm, sufficient to resolve the main features of the

deformation process in our experiments. Previously, further microstructural analysis has been chiefly based on optical and SEM imaging of deformed samples [e.g., *Nasseri et al.*, 2006; *Fredrich et al.*, 1995]. Here, we have used X-ray CT scanner technology, a non-destructive technique, to investigate deformation features post-test. Preliminary 2D micro-CT images show that sub-millimetre scale features are well-imaged. Figure 3 also shows that AE locations of individual fracture events match the micro-CT images of the deformation zone very well. The application of the combined AE/CT approach is of particular interest in the field of volcano tectonics, as the rates of detected VT events under magmatic pressures are intimately related to the slow extension of fractures within the volcanic edifices [Kilburn, 2003]. In such a scenario, the rock mass is already damaged with microcracks, and may also contain vugs and large pores due to degassing. We have demonstrated a link between wave velocity changes, evolution of AE patterns and evolving crack damage in our experiments. At the volcano scale, linking changing seismic velocities and seismicity with evolving deformation fabric can play a key role in interpreting seismic precursors to instability. In addition, knowledge of the complex and poorly understood micromechanical coupling between crack damage and volcanic fluids (magma and gas) and its evolution under stress has important implications for interpreting seismic signals routinely measured on volcanic edifices.

[15] In conclusion, we demonstrate that we have been able to use full waveform AE location to follow the complete temporal evolution of crack damage to produce a localized fault zone in a volcanic rock with a high level of pre-existing crack damage. We also show that the faulting process in such a rock is slower than in other crystalline rocks without such damage. The period of stress decrease between the peak stress and the dynamic stress drop is associated with a marked increase in AE activity over several tens of seconds. This period coincides with the development of the throughgoing fault, and the dynamic stress drop that signifies macroscopic failure only occurs after the fault zone has completely traversed the sample. We find excellent agreement between AE locations of individual microcracks and the post-test micro-CT image of the fault zone.

[16] **Acknowledgments.** This work was partially supported by a Marie-Curie International Fellowship within the 6th European Community Framework programme (contract MOIF-CT-2005-020167 to PMB) and partially supported by a Natural Sciences and Engineering Research Council (NSERC) discovery grant to RPY. The authors kindly thank Sergei Stanchits and Alexandre Schubnel for constructive comments that greatly improved the manuscript, and Edward Townend at UCL for assistance with setting up the experiments.

References

- Ayling, M. R., P. G. Meredith, and S. A. F. Murrell (1995), Microcracking during triaxial deformation of porous rocks monitored by changes in rock physical properties: 1. Elastic-wave propagation measurements on dry rocks, *Tectonophysics*, *245*, 205–221.
- Benson, P., A. Schubnel, S. Vinciguerra, C. Trovato, P. Meredith, and R. P. Young (2006), Modeling the permeability evolution of microcracked rocks from elastic wave velocity inversion at elevated isostatic pressure, *J. Geophys. Res.*, *111*, B04202, doi:10.1029/2005JB003710.
- Burlini, L., S. Vinciguerra, G. Di Toro, G. De Natale, P. G. Meredith, and J.-P. Burg (2007), Seismicity preceding volcanic eruptions: New experimental insights, *Geology*, in press.
- Chouet, B. (2003), Volcano seismology, *Pure Appl. Geophys.*, *160*, 739–788.
- Collier, L., and J. Neuberg (2006), Incorporating seismic observations into 2D conduit flow modeling, *J. Volcanol. Geotherm. Res.*, *152*, 331–346.
- Eccles, D., P. R. Sammonds, and O. C. Clint (2005), Laboratory studies of electrical potential during rock failure, *Int. J. Rock Mech. Min. Sci.*, *42*, 900–910.
- Elsworth, D., and S. J. Day (1999), Flank collapse triggered by intrusion: The Canarian and Cape Verde Archipelagoes, *J. Volcanol. Geotherm. Res.*, *94*, 323–340.
- Fredrich, J. T., B. Menendez, and T.-F. Wong (1995), Imaging the pore structure of geomaterials, *Science*, *268*, 276–279.
- Ketcham, R. A., and W. D. Carlson (2001), Acquisition, optimization and interpretation of X-ray computed tomographic imagery: Applications to the geosciences, *Comput. Geosci.*, *27*, 381–400.
- Kilburn, C. R. J. (2003), Multiscale fracturing as a key to forecasting volcanic eruptions, *J. Volcanol. Geotherm. Res.*, *125*, 271–289.
- Lei, X., K. Kusunose, M. V. M. S. Rao, O. Nishizawa, and T. Satoh (2000), Quasi-static fault growth and cracking in homogeneous brittle rock under triaxial compression using acoustic emission monitoring, *J. Geophys. Res.*, *105*(B3), 6127–6140.
- Lockner, D. A., J. D. Byerlee, V. Kukusenko, A. Ponomarev, and A. Sidorin (1991), Quasi-static fault growth and shear fracture energy in granite, *Nature*, *350*, 39–42.
- Louis, L., T.-F. Wong, P. Baud, and S. Tempe (2006), Imaging strain localization by X-ray computed tomography: Discrete compaction bands in Diemelstadt sandstone, *J. Struct. Geol.*, *28*, 762–775.
- McNutt, S. R. (1996), Seismic monitoring and eruption forecasting of volcanoes: A review of the state-of-the-art and case histories, in *Monitoring and Mitigation of Volcano Hazards*, edited by R. Scarpa and R. Tilling, pp. 99–146, Springer, New York.
- Meredith, P. G., I. G. Main, and C. Jones (1990), Temporal variations in seismicity during quasi-static and dynamic rock failure, *Tectonophysics*, *175*, 249–268.
- Nasseri, M. H. B., B. Mohanty, and R. P. Young (2006), Fracture toughness measurements and acoustic emission activity in brittle rocks, *Pure Appl. Geophys.*, *163*, 1–29.
- Neuberg, J. W., H. Tuffen, L. Collier, D. Green, T. Powell, and D. Dingwell (2006), The trigger mechanism of low-frequency earthquakes on Montserrat, *J. Volcanol. Geotherm. Res.*, *153*, 37–50.
- Stanchits, S., S. Vinciguerra, and G. Dresen (2006), Ultrasonic velocities, acoustic emission characteristics and crack damage of basalt and granite, *Pure Appl. Geophys.*, *163*, 974–993.
- Thompson, B. D. (2006), Acoustic emission investigation of fracture and fault mechanics in the laboratory, Ph.D. thesis, 194 pp., Univ. of Liverpool, Liverpool, U. K.
- Thompson, B. D., R. P. Young, and D. A. Lockner (2005), Observations of premonitory acoustic emission and slip nucleation during a stick slip experiment in smooth faulted Westerly granite, *Geophys. Res. Lett.*, *32*, L10304, doi:10.1029/2005GL022750.
- Thompson, B. D., R. P. Young, and D. A. Lockner (2006), Fracture in Westerly granite under AE feedback and constant strain rate loading: Nucleation, quasi-static propagation, and the transition to unstable fracture propagation, *Pure Appl. Geophys.*, *163*, 995–1019.
- Tricart, J. P., M. Van Geet, and A. Sasov (2000), Using Micro-CT for 3D characterization of geological materials, *Microsc. Anal.*, *14*, 31.
- Vinciguerra, S., D. Elsworth, and S. Malone (2005a), The 1980 pressure response and flank failure of Mount St. Helens (USA) inferred from seismic scaling exponents, *J. Volcanol. Geotherm. Res.*, *144*, 155–168.
- Vinciguerra, S., C. Trovato, P. G. Meredith, and P. M. Benson (2005b), Relating seismic velocities, thermal cracking and permeability in Mt. Etna and Iceland basalts, *Int. J. Rock Mech. Min. Sci.*, *42*, 900–910.
- Voight, B., and D. Elsworth (1997), Failure of volcano slopes, *Geotechnique*, *47*, 1–31.

P. M. Benson and P. G. Meredith, Mineral, Ice and Rock Physics Laboratory, Department of Earth Sciences, University College London, Gower Street, London WC1E 6BT, UK. (p.benson@ucl.ac.uk)

B. D. Thompson and R. P. Young, Lassonde Institute, University of Toronto, 170 College Street, Toronto, ON, Canada M5S 3E3.

S. Vinciguerra, High Pressure High Temperature Laboratory of Experimental Volcanology and Geophysics, Department of Seismology and Tectonophysics, Istituto Nazionale di Geofisica e Vulcanologia, Via di Vigna Murata 605, I-00143 Rome, Italy.